Chemical Science

ROYAL SOCIETY OF CHEMISTRY

EDGE ARTICLE

View Article Online
View Journal

Cite this: DOI: 10.1039/d5sc09403h

All publication charges for this article have been paid for by the Royal Society of Chemistry

Chloride-induced easier phase transformation and catalytic synergy for enhanced seawater splitting

Haibin Ma,[a] Yuxiang Jin,[b] Xiaoyan Zhou,[a] Yujie Cui,[a] Yang Zhao,[c] Chia-Yu Chang,[d] Min-Hsin Yeh,[e] Wei-Hsiang Huang,*[fg] Erhong Song,*[h] Jiwei Ma*[a] and Hongfei Cheng*[a]

Hydrogen production from sustainable seawater splitting technology is restricted by the side reactions of chlorine evolution and chlorine oxidation on the anode. Different from the common catalyst design strategy, *i.e.*, selecting materials repelling chloride ions, herein, we find that the strong adsorption of chloride ions on noble metals can be an advantage. We design a heterostructure catalyst consisting of atomically dispersed Ru doped IrO_x nanoclusters/α-$Co(OH)_2$ nanosheets. This as-synthesized catalyst only requires an overpotential of 206 mV to drive 100 mA cm^{-2}, and it can withstand continuous catalysis for as long as 310 h under 500 mA cm^{-2}. *In situ* spectroscopy and theoretical calculations show that Cl^- ion adsorption on IrO_x clusters at low overpotentials promotes the phase transition of α-$Co(OH)_2$ to CoOOH, lowering the OER barrier at the Ru site and resulting in a significantly reduced theoretical overpotential of 200 mV for Ru-IrO_x-Cl/CoOOH. Our work demonstrates a catalyst with Cl^- adsorption-promoted OER activity, in contrast to the traditional Cl^- repelling catalyst design strategy for seawater splitting.

Received 2nd December 2025
Accepted 12th March 2026

DOI: 10.1039/d5sc09403h

rsc.li/chemical-science

Introduction

Seawater accounts for ~97% of global water, hence electrochemical seawater splitting is widely recognized as an economical and sustainable route to producing high-quality hydrogen.[1–3] One challenge of electrochemical seawater splitting is the accompanying side reactions of the Cl^- oxidation reaction (CLOR) occurring on the anode, which can produce Cl_2 or hypochlorite, seriously poisoning catalytic active centers and corroding the anode materials.[4–8] The standard electrode potential (SEP) gap between the OER and CLOR is pH-dependent. Fortunately, when the pH value is above 7.5, the SEP of the CLOR is 1.72 V,[9–11] much higher than that of the OER. Besides, the OER is more kinetically favorable under alkaline conditions than acidic or neutral conditions. Therefore, the investigation on suitable catalysts toward large-current seawater splitting is usually conducted under alkaline conditions.[12–14] Alkaline conditions also allow for the utilization of earth-abundant metals, widening the choice of catalysts and lowering the cost of water splitting.

3d transition metal hydroxides are promising alternatives to the commercial Ir/Ru-based materials for alkaline OER,[15–18] but they are prone to be corroded by Cl^- ions during seawater splitting. A common strategy to improve their stability is constructing a protective layer to repel Cl^- adsorption. The protective layer is likely to cover the active sites for the OER and this strategy may become ineffective at high overpotentials for large current generation, at which the driving force of Cl^- adsorption becomes stronger. Instead of repelling Cl^- ions, very recent studies have demonstrated that the strong Cl adsorption on noble metals could be beneficial for designing catalysts based on transition metal hydroxides. For example, Duan *et al.*[19] found that Cl^- adsorption on Ir single atoms can modulate the electronic structure of active sites and lower the OER activation energy of Ir/cobalt iron layered double hydroxide. However, adsorbing too many Cl^- ions on noble-metal sites may hinder the adsorption of oxygen-containing intermediates and limit the overall OER kinetics. Moreover, the coordination between

[a]*Shanghai Key Laboratory for R&D and Application of Metallic Functional Materials, Institute of New Energy for Vehicles, School of Materials Science and Engineering, Tongji University, Shanghai 201804, P. R. China. E-mail: jiwei.ma@tongji.edu.cn; cheng_hongfei@tongji.edu.cn*

[b]*Key Laboratory of Automobile Materials, School of Materials Science and Engineering, Jilin University, Changchun 130025, P. R. China*

[c]*Dalian National Laboratory for Clean Energy (DNL), Dalian Institute of Chemical Physics, Chinese Academy of Science, Dalian 116023, P. R. China*

[d]*Graduate Institute of Applied Science and Technology, National Taiwan University of Science and Technology, Taipei 106, Taiwan*

[e]*Department of Chemical Engineering, National Taiwan University of Science and Technology, Taipei 106, Taiwan*

[f]*Sustainable Electrochemical Energy Development (SEED) Center, National Taiwan University of Science and Technology, Taipei 106, Taiwan*

[g]*National Synchrotron Radiation Research Center (NSRRC), Hsinchu, 300092, Taiwan. E-mail: huang.sean@nsrrc.org.tw*

[h]*State Key Laboratory of High Performance Ceramics, Shanghai Institute of Ceramics, Chinese Academy of Sciences, Shanghai 201899, P. R. China. E-mail: ehsong@mai.sic.ac.cn*

Cl^- and noble metals still has the potential of generating Cl_2 or hypochlorite, especially at high overpotentials.[20] An ideal catalyst should be able to desorb Cl^- at high overpotentials so as to completely avoid the CLOR and fully expose active sites for the OER.[21] This inspires us to design a heterostructured catalyst composed of transition metal hydroxides and noble metals, which possesses a Cl^- adsorption capacity inversely correlated with the overpotential. More specifically, the designed catalyst has a strong Cl^- adsorption on noble metal sites at lower overpotentials, which can lower the OER energy barrier, whereas it has a weak Cl^- adsorption at higher overpotentials, which can facilitate water adsorption for larger current generation.[22]

Herein, we developed a heterostructure catalyst comprising of atomically dispersed Ru-doped IrO_x nanoclusters and α-$Co(OH)_2$ nanosheets (denoted as Ru-IrO_x/α-$Co(OH)_2$) for electrochemical seawater splitting. At low potentials, Cl^- prefers to adsorb on the IrO_x clusters, which facilitates the phase transformation of $Co(OH)_2$ into highly active CoOOH and promotes the OER on the atomically dispersed Ru sites. At high potentials, water adsorption increases and Cl^- ion adsorption decreases, releasing the active sites for the OER and preventing the CLOR side reactions, as illustrated in Fig. 1a and proved by *in situ* spectroscopy experiments as well as density functional theory (DFT) calculations. The as-fabricated catalyst exhibited enhanced OER activity with an overpotential of 206 mV to drive

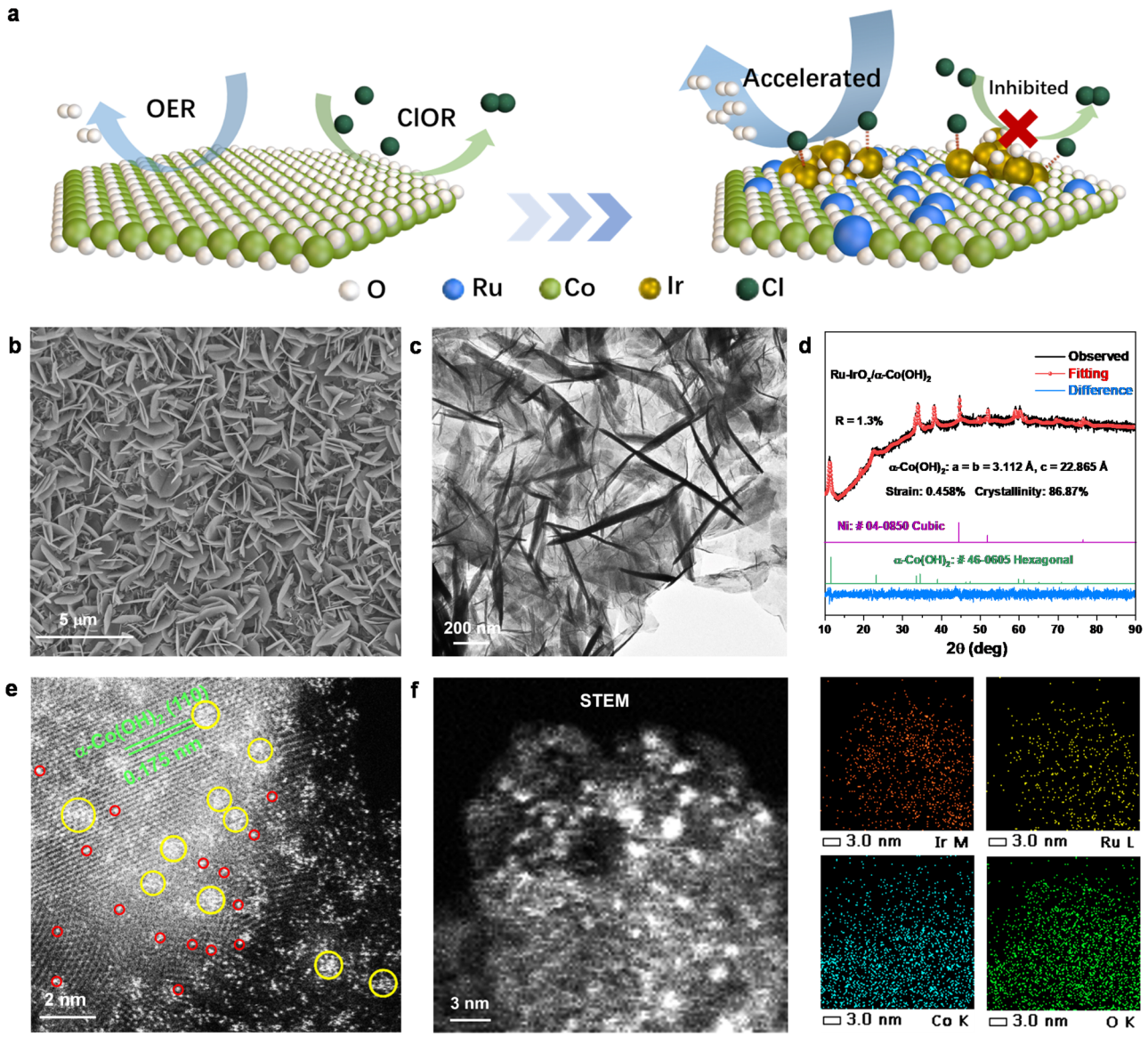

Fig. 1 (a) Illustration of the structure of the Ru-IrO_x/α-$Co(OH)_2$ catalyst and its corresponding OER kinetics promoting and CLOR repelling effects. (b) SEM image, (c) TEM image, and (d) XRD pattern of the Ru-IrO_x/α-$Co(OH)_2$ catalyst. (e) HAADF-STEM image of the Ru-IrO_x/α-$Co(OH)_2$ catalyst, where many nanoclusters and isolated atoms dispersed on the α-$Co(OH)_2$ surface were obviously observed and marked with yellow and red circles, respectively. (f) STEM image and corresponding EDS elemental mapping of the Ru-IrO_x/α-$Co(OH)_2$ catalyst.

100 mA cm^{-2}, and remained stable during 310 h catalysis under 500 mA cm^{-2} in 1.0 M KOH + seawater electrolyte.

Synthesis and characterization of catalysts

The Ru-IrO_x/α-$Co(OH)_2$ heterostructure catalyst was synthesized *via* a facile two-step process. Firstly, layered α-$Co(OH)_2$ nanosheets (denoted as α-$Co(OH)_2$) (Fig. S1 and S2) were prepared by an electrodeposition method using nickel foam as a substrate. Subsequently, the as-obtained α-$Co(OH)_2$ nanosheets were immersed in an $IrCl_3$/$RuCl_3$ mixed aqueous solution with an atomic ratio of Ir^{3+}/Ru^{3+} of 5/1, thus IrO_x cluster/α-$Co(OH)_2$ nanosheet heterostructure doped with atomically dispersed Ru, *i.e.*, Ru-IrO_x/α-$Co(OH)_2$, was obtained. The scanning electron microscopy (SEM) images in Fig. 1b and S3 show that the nanosheets were vertically and homogeneously grown on nickel foam. The low-magnification transmission electron microscopy (TEM) image in Fig. 1c shows that the nanosheet surface did not become obviously rough after impregnation treatment. The X-ray diffraction (XRD) pattern in Fig. 1d illustrates that a layered α-$Co(OH)_2$ phase with hexagonal structure and cubic Ni phase were observed. The XRD refinement result in Fig. 1d shows that the α-$Co(OH)_2$ phase has crystal parameters: $a = b =$ 3.112 Å, $c =$ 22.865 Å. The cubic Ni phase was derived from the Ni foam substrate when exfoliating the Ru-IrO_x/α-$Co(OH)_2$ powder from the self-supporting electrode using the ultrasound technique. The high angle annular dark field scanning TEM (HAADF-STEM) images in Fig. 1e and S4 show that abundant nanoclusters (circled in yellow) and isolated atoms (circled in red) are homogeneously distributed on the α-$Co(OH)_2$ surface. The line-scan profile in Fig. S5 indicates that the nanoclusters are composed of Ir species and Ru species. Based on inductively coupled plasma optical emission spectroscopy (ICP-OES), the total mass loading amount of Ir and Ru in the Ru-IrO_x/α-$Co(OH)_2$ catalyst approaches 0.92 wt% and the corresponding atomic ratio of Ir/Ru approaches 15.5/1, indicating the clusters are mainly composed of Ir species. Energy dispersive spectroscopy (EDS) mapping images in Fig. 1f indicate that Ru, Ir, Co and O elements were homogeneously distributed. For comparison, RuO_x/α-$Co(OH)_2$ (Fig. S6) and IrO_x/α-$Co(OH)_2$ (Fig. S7) catalysts were also prepared as the control groups using a similar synthesis procedure.

Electronic properties and coordination environment

The composition and electronic structure of catalysts were studied by X-ray photoelectron spectroscopy (XPS). The detailed XPS fitting parameters are listed in Table S1. For the Ru-IrO_x/α-$Co(OH)_2$ catalyst, the high-resolution Ru 3p XPS spectrum in Fig. S8a shows a strong peak locating at 486.2 eV, assigned to the $3p_{1/2}$ of Ru^{4+} ions,[23–26] which is consistent with the observation of high-resolution Ru 3d XPS spectra in Fig. S8b. The high-resolution Ir 4f XPS spectrum in Fig. S8c shows three peaks located at 60.6, 62.4 and 65.6 eV, corresponding to Co 3p, Ir^{4+} $4f_{7/2}$ and Ir^{4+} $4f_{5/2}$, respectively.[27–29] In the high-resolution Co 2p XPS spectrum (Fig. S8d), the two major peaks located at 780.9 and 796.5 eV are assigned to $2p_{3/2}$ and $2p_{1/2}$ of Co^{3+} ions,[30,31] and the two fitted peaks located at 782.4 and 798.3 eV are ascribed to $2p_{3/2}$ and $2p_{1/2}$ of Co^{2+} ions. Compared with the IrO_x/α-$Co(OH)_2$ catalyst, the Ir^{4+} $4f_{7/2}$ and Co^{3+} $2p_{3/2}$ XPS peaks in the Ru-IrO_x/α-$Co(OH)_2$ catalyst shifted to lower binding energy values by 0.19 and 0.41 eV, respectively. The high-resolution O 1s XPS spectrum in Fig. S8e indicates the existence of metal–O, metal–OH, and H–O–H bonds and oxygen vacancies.[32–34]

The fine coordination environment of catalysts was studied by X-ray absorption spectroscopy (XAS). In detail, the X-ray absorption near-edge spectroscopy (XANES) spectra at the Co–K edge show that the oxidation state of Co in RuO_x/α-$Co(OH)_2$, IrO_x/α-$Co(OH)_2$, Ru-IrO_x/α-$Co(OH)_2$ catalysts was very close to +2 (Fig. 2a). The corresponding extended X-ray absorption fine-structure (EXAFS) spectra at the Co–K edge show two dominant peaks: the one locating at around 1.4 Å was assigned to a Co–O bond, and the other one locating at around 2.6 Å was assigned to a Co–Co bond (Fig. 2b, S9 and Table S2). The XANES spectra at the Ir-L_3 edge show that the Ir oxidation state in IrO_x/α-$Co(OH)_2$ and Ru-IrO_x/α-$Co(OH)_2$ catalysts was very close to +4 (Fig. 2c). The corresponding EXAFS spectra of IrO_x/α-$Co(OH)_2$ and Ru-IrO_x/α-$Co(OH)_2$ heterostructures at the Ir-L_3 edge show one dominant peak at around 1.6 Å (Fig. 2d), which was assigned to the Ir–O bond, indicating that the Ir species in the above two heterostructures were mainly IrO_x clusters. The small peak in Fig. 2d locating at around 2.9 Å was attributed to Ir–Ir bonds. The EXAFS fitting of Ru-IrO_x/α-$Co(OH)_2$ at the Ir-L_3 edge implies that there are some Ru atoms doped in IrO_x clusters (Fig. S10 and Table S3). The XANES spectra at the Ru–K edge show that the Ru oxidation state in RuO_x/α-$Co(OH)_2$ and Ru-IrO_x/α-$Co(OH)_2$ catalysts was very close to +4 (Fig. 2e), and the corresponding EXAFS spectra (Fig. 2f, S11 and Table S4) show one dominant peak at around 1.6 Å, which is assigned to the Ru–O bond. The atomically dispersed Ru was further confirmed by wavelet transform of the Ru–K edge, where only one strong peak corresponding to the Ru–O bond was observed in RuO_x/α-$Co(OH)_2$ (Fig. 2g) and Ru-IrO_x/α-$Co(OH)_2$ (Fig. 2h), whereas another peak corresponding to the Ru–Ru bond was also obviously found in the RuO_2 reference (Fig. 2i). In the EXAFS spectra at the Co–K edge, the peaks corresponding to the Co–O and Co–Co bonds in the Ru-IrO_x/α-$Co(OH)_2$ catalyst shifted to a higher radical distance compared with that in the IrO_x/α-$Co(OH)_2$ catalyst, indicating lattice expansion of α-$Co(OH)_2$ after the incorporation of atomically dispersed Ru. In contrast, in the EXAFS spectra at the Ir-L_3 edge, the Ir–O and Ir–Ir peaks of the Ru-IrO_x/α-$Co(OH)_2$ catalyst shifted to lower radical distance compared with that of the IrO_x/α-$Co(OH)_2$ catalyst, indicating lattice contraction of IrO_x clusters after atomically dispersed Ru incorporation. The above analysis indicated that atomically dispersed Ru was distributed in both α-$Co(OH)_2$ nanosheets and IrO_x clusters; therefore, the coordination environment of O–Co–O and O–Ir–O was efficiently modulated by introducing atomically dispersed Ru species.

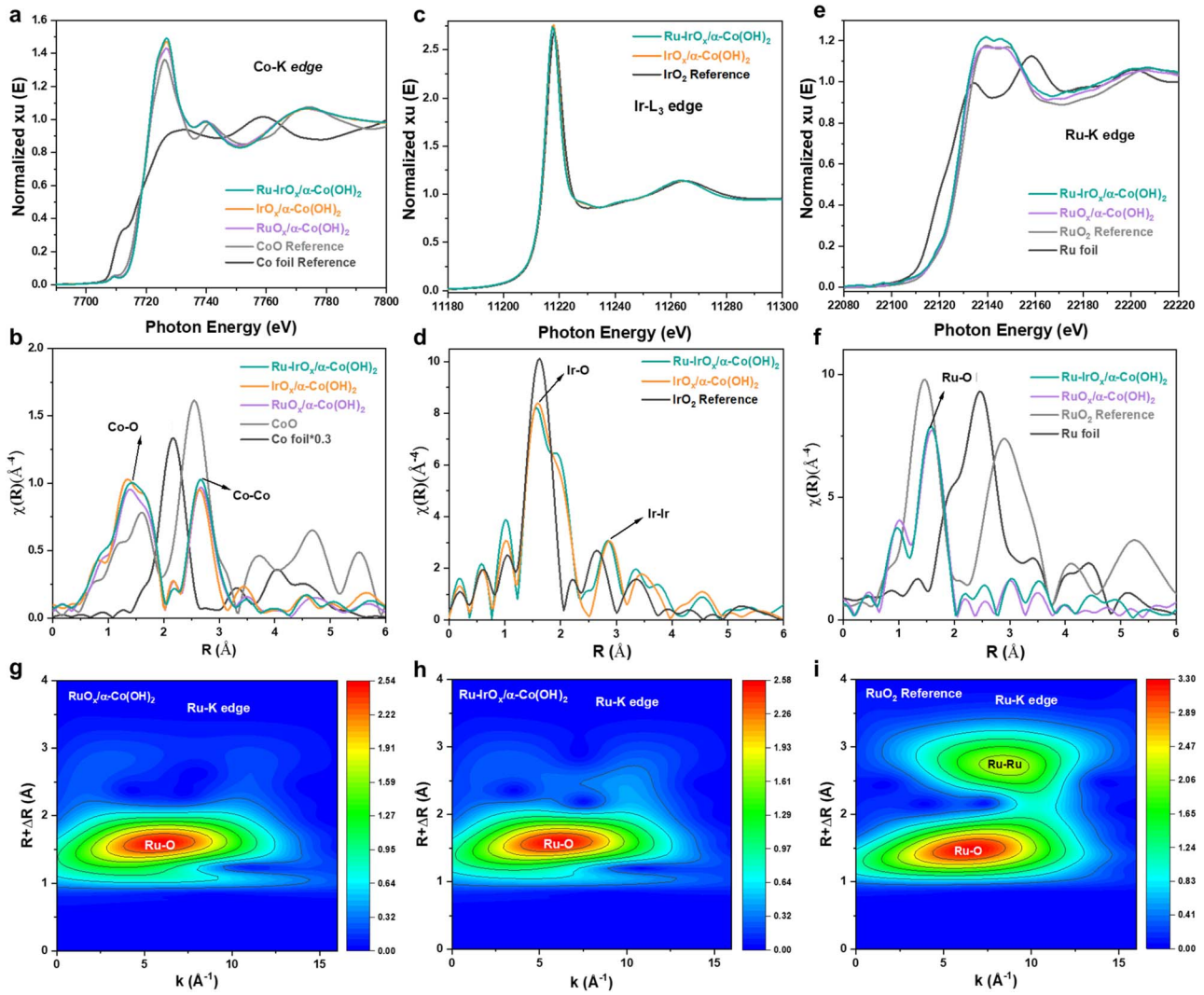

Fig. 2 (a) XANES spectra and (b) EXAFS spectra of the Co–K edge for IrO_x/α-$Co(OH)_2$, RuO_x/α-$Co(OH)_2$, Ru-IrO_x/α-$Co(OH)_2$, and CoO and Co foil references. (c) XANES spectra and (d) EXAFS spectra of the Ir-L_3 edge for IrO_x/α-$Co(OH)_2$, Ru-IrO_x/α-$Co(OH)_2$, and IrO_2 and Ir foil references. (e) XANES spectra and (f) EXAFS spectra of the Ru–K edge for RuO_x/α-$Co(OH)_2$, Ru-IrO_x/α-$Co(OH)_2$, and RuO_2 and Ru foil references. Wavelet transform of the Ru–K edge for (g) RuO_x/α-$Co(OH)_2$, (h) Ru-IrO_x/α-$Co(OH)_2$, and (i) RuO_2 reference.

Electrochemical performance evaluation

The catalytic performance of the Ru-IrO_x/α-$Co(OH)_2$ heterostructure was evaluated using a traditional three-electrode system in a N_2-saturated alkaline seawater electrolyte, with 1.0 M KOH dissolved in different salinized artificial seawater samples. Linear sweep voltammetry (LSV) curves in Fig. 3a show that the Ru-IrO_x/α-$Co(OH)_2$ catalyst exhibited the best OER activity in 1.0 M KOH + seawater electrolyte. It only required an overpotential of 206 mV to deliver 100 mA cm^{-2} (Fig. 3b), much lower than those of IrO_x/α-$Co(OH)_2$ (257 mV), RuO_x/α-$Co(OH)_2$ (323 mV), α-$Co(OH)_2$ (380 mV) and commercial IrO_2 (454 mV) catalysts. The overpotential difference was enlarged as the current density increased to 500 mA cm^{-2}. Electrochemical active surface area (ECSA) evaluation was conducted to identify the origin of the enhanced catalysis. The Ru-IrO_x/α-$Co(OH)_2$ catalyst has higher double layer capacitance (Fig. S12) than IrO_x/α-$Co(OH)_2$, corresponding to higher ECSA[35,36] of Ru-IrO_x/α-$Co(OH)_2$ (132.3 cm^2) than IrO_x/α-$Co(OH)_2$ (85.4 cm^2), indicating that the number of active sites increased after Ru doping. The ECSA normalized LSV curves in Fig. 3c show that the Ru-IrO_x/α-$Co(OH)_2$ catalyst exhibited enhanced OER intrinsic activity than IrO_x/α-$Co(OH)_2$, RuO_x/α-$Co(OH)_2$ and α-$Co(OH)_2$ catalysts. Electrochemical impedance spectroscopy (EIS) measurements were conducted to investigate the charge transfer properties of catalysts. The Nyquist plot in Fig. 3d shows that the Ru-IrO_x/α-$Co(OH)_2$ catalyst possessed lower charge-transfer resistance than IrO_x/α-$Co(OH)_2$, RuO_x/α-$Co(OH)_2$ and α-$Co(OH)_2$ catalysts. The as-synthesized Ru-IrO_x/α-$Co(OH)_2$ catalyst had a Tafel slope of 68.8 mV dec^{-1} (Fig. 3e) in the kinetic region, which was much lower than those of RuO_x/α-$Co(OH)_2$ (137.4 mV dec^{-1}), IrO_x/α-$Co(OH)_2$ (117.7 mV dec^{-1}), α-$Co(OH)_2$ (143.5 mV dec^{-1}), and commercial IrO_2 (169.7 mV dec^{-1}) catalysts, indicating that

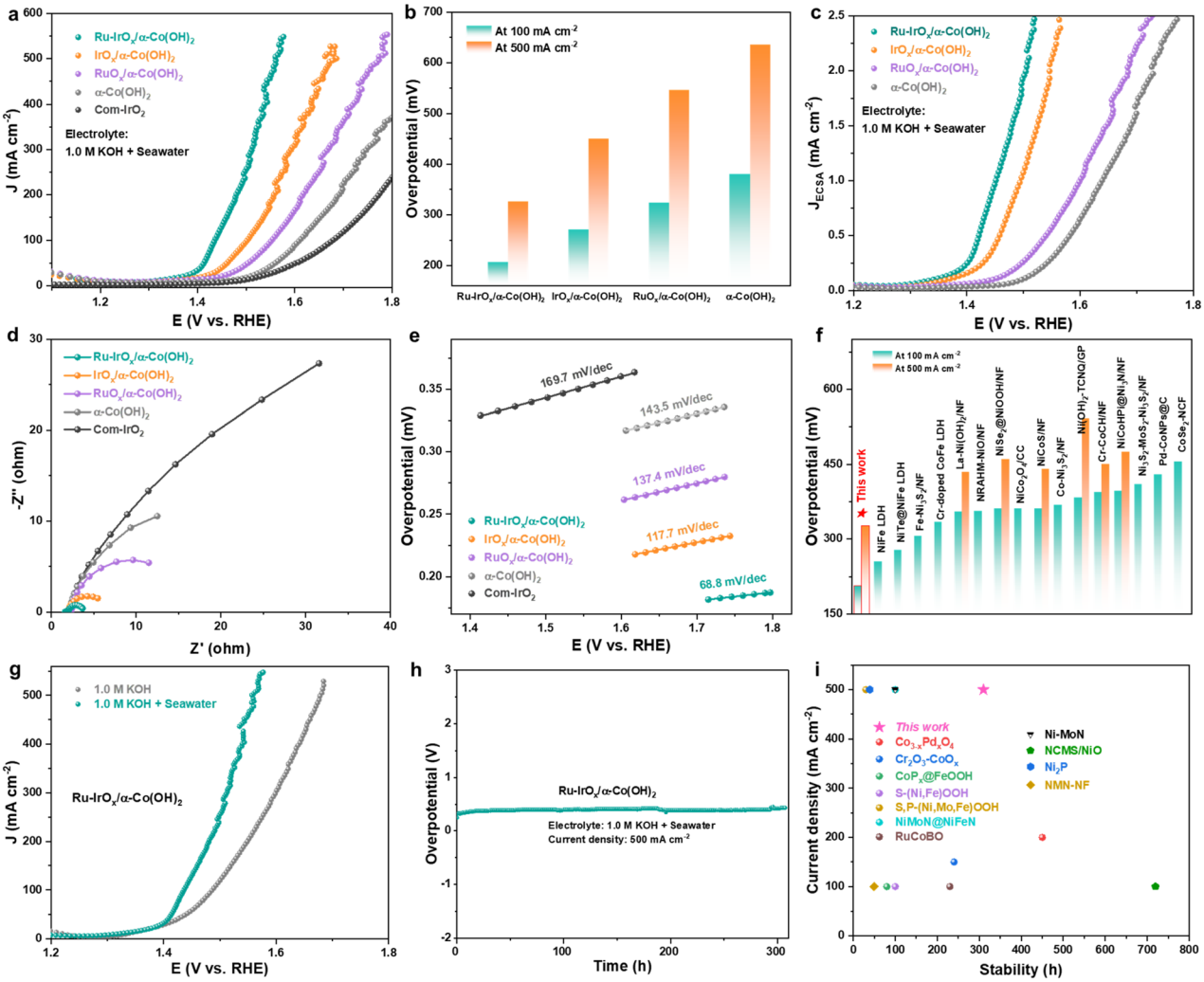

Fig. 3 Electrocatalytic performance evaluation. (a) OER polarization curves for α-$Co(OH)_2$, IrO_x/α-$Co(OH)_2$, RuO_x/α-$Co(OH)_2$, Ru-IrO_x/α-$Co(OH)_2$ and commercial IrO_2 catalysts. Electrolyte: 1.0 M KOH + seawater. (b) Comparison of the overpotentials at 100 mA cm^{-2} and 500 mA cm^{-2} for different electrocatalytic materials obtained from the OER polarization curves in panel (a). (c) Polarization curves of α-$Co(OH)_2$, IrO_x/α-$Co(OH)_2$, RuO_x/α-$Co(OH)_2$ and Ru-IrO_x/α-$Co(OH)_2$ catalysts normalized to corresponding ECSA. (d) Comparison of EIS spectra for α-$Co(OH)_2$, IrO_x/α-$Co(OH)_2$, RuO_x/α-$Co(OH)_2$, Ru-IrO_x/α-$Co(OH)_2$ and commercial IrO_2 catalysts. (e) Comparison of Tafel slopes obtained from the OER polarization curves in panel (a). (f) Comparison of the overpotentials of Ru-IrO_x/α-$Co(OH)_2$ at 100 and 500 mA cm^{-2} with recently reported catalysts in 1.0 M KOH + seawater electrolyte. (g) Comparison of OER polarization curves for the Ru-IrO_x/α-$Co(OH)_2$ catalyst in different electrolytes, including 1.0 M KOH and 1.0 M KOH + seawater. (h) Durability evaluation of the Ru-IrO_x/α-$Co(OH)_2$ catalyst at 500 mA cm^{-2} in 1.0 M KOH + seawater electrolyte. (i) Stability comparison of the Ru-IrO_x/α-$Co(OH)_2$ catalyst with recently reported catalysts in 1.0 M KOH + seawater electrolyte.

significantly enhanced catalysis occurred on the Ru-IrO_x/α-$Co(OH)_2$ catalyst. The overpotentials of the RuO_x/α-$Co(OH)_2$ catalyst at 100 and 500 mA cm^{-2} in 1.0 M KOH + seawater electrolyte were much lower than those of recently reported catalysts (Fig. 3f and Table S5). The influence of Ru doping content on alkaline seawater oxidation performance was also investigated. We prepared Ru-IrO_x/α-$Co(OH)_2$ catalysts with different IrO_x and RuO_x loading amounts, and it was found that the Ru-IrO_x/α-$Co(OH)_2$ catalyst synthesized with an Ir^{3+}/Ru^{3+} molar ratio of 5/1 (Fig. S13) exhibited optimal catalytic activity. We have evaluated the selectivity of the Ru-IrO_x/α-$Co(OH)_2$ catalyst toward the OER in 1.0 M KOH + seawater electrolyte using a rotating ring disk electrode (RRDE). As shown in Fig. S14, the Faraday efficiency of the Ru-IrO_x/α-$Co(OH)_2$ catalyst toward the OER was more than 90%.

Furthermore, by comparing the OER performance in 1.0 M KOH and 1.0 M KOH + seawater electrolyte, it was found that the Cl^- ions in seawater can efficiently promote alkaline OER kinetics of the Ru-IrO_x/α-$Co(OH)_2$ catalyst (Fig. 3g). This phenomenon was further confirmed when decreasing the salinity of seawater (Fig. S15). To directly observe the function of Cl^- ions in promoting alkaline OER kinetics, *in situ* Fourier transform infrared spectroscopy (FTIR) was conducted on the Ru-IrO_x/α-$Co(OH)_2$ catalyst both in 1.0 M KOH and 1.0 M KOH + seawater electrolytes. As shown in Fig. S16, the intensity of peaks corresponding to adsorbed *OH species obviously

strengthened in 1.0 M KOH + seawater compared with that in 1.0 M KOH, and the above two peaks intensified as the operating potentials increased from 1.20 V *vs.* RHE to 1.70 V *vs.* RHE, indicating that the water molecules can be dissociated more easily after introducing seawater in alkaline electrolyte.

As for the stability evaluation of the Ru-IrO_x/α-$Co(OH)_2$ catalyst, negligible overpotential degradation was observed at 500 mA cm^{-2} for 310 h in the electrolyte of 1.0 M KOH + seawater (Fig. 3h), indicating the robustness of our as-synthesized Ru-IrO_x/α-$Co(OH)_2$ catalyst for alkaline seawater oxidation. The stability performance surpassed that of most recently reported catalysts (Fig. 3i). The Ru mass ratio in the spent Ru-IrO_x/α-$Co(OH)_2$ catalyst was 0.014%, as confirmed by ICP, indicating the existence of Ru species after stability evaluation. Fig. S17 shows that the electronic structure of the Ru-IrO_x/α-$Co(OH)_2$ catalyst experienced negligible destruction except that it slightly shifts to higher binding energy values after the alkaline seawater oxidation stability test, which was ascribed to surface reconstruction under the OER operating potential.[37,38] The morphology and microstructure of our as-synthesized Ru-IrO_x/α-$Co(OH)_2$ catalyst were retained after long-term catalysis operation (Fig. S18), indicating its structural stability.

Understanding the mechanism

To investigate the mechanism of the Ru-IrO_x/α-$Co(OH)_2$ heterostructure for enhanced OER catalysis, we performed *in situ* XAS characterization in the electrolyte of 1.0 M KOH + seawater. As shown in Fig. 4a, when the operating voltage increased from open circuit potential (OCP) to 1.3 V *vs.* RHE, the phonon energy for the Ir-L_3 absorption edge shifted toward higher energy values (inset in Fig. 4a), indicating the higher valence state of Ir species, which was ascribed to the oxidation of IrO_x clusters. As the operating voltage increased from 1.3 V *vs.* RHE to 1.5 V *vs.* RHE, further phonon energy shifts of the Ir-L_3 adsorption edge toward higher energy values were observed, and the energy shifts disappeared when the voltage was cut off. As for the variation of the coordination environment (Fig. 4b), apart from the inherent Ir–O bonds existing in the Ru-IrO_x/α-$Co(OH)_2$ heterostructure, Ir–Cl bonds locating at around 2.0 Å were clearly observed under OCP and 1.3 V *vs.* RHE, indicating that Cl^- ions were adsorbed on IrO_x clusters in the alkaline seawater medium. When the applied potential increased from OCP to 1.3 V *vs.* RHE, the fitting results of the EXAFS spectra of Ru-IrO_x/α-$Co(OH)_2$ at the Ir-L_3 edge show that the Ir–Cl coordination number slightly decreased and the Ir–Cl radial distance slightly increased (Fig. S19, S20 and Tables S6, S7), which implies a weaker Cl adsorption on IrO_x clusters. The intensity of Ir–Cl bonds obviously weakened when the operating voltage reached 1.5 V *vs.* RHE, indicating high-valent chlorine compounds such as ClO^- or ClO_3^- are unlikely to be generated at high overpotentials. Fig. S21 shows the wavelet transforms for the Ir-L_3 edge in IrO_x clusters under *in situ* operating

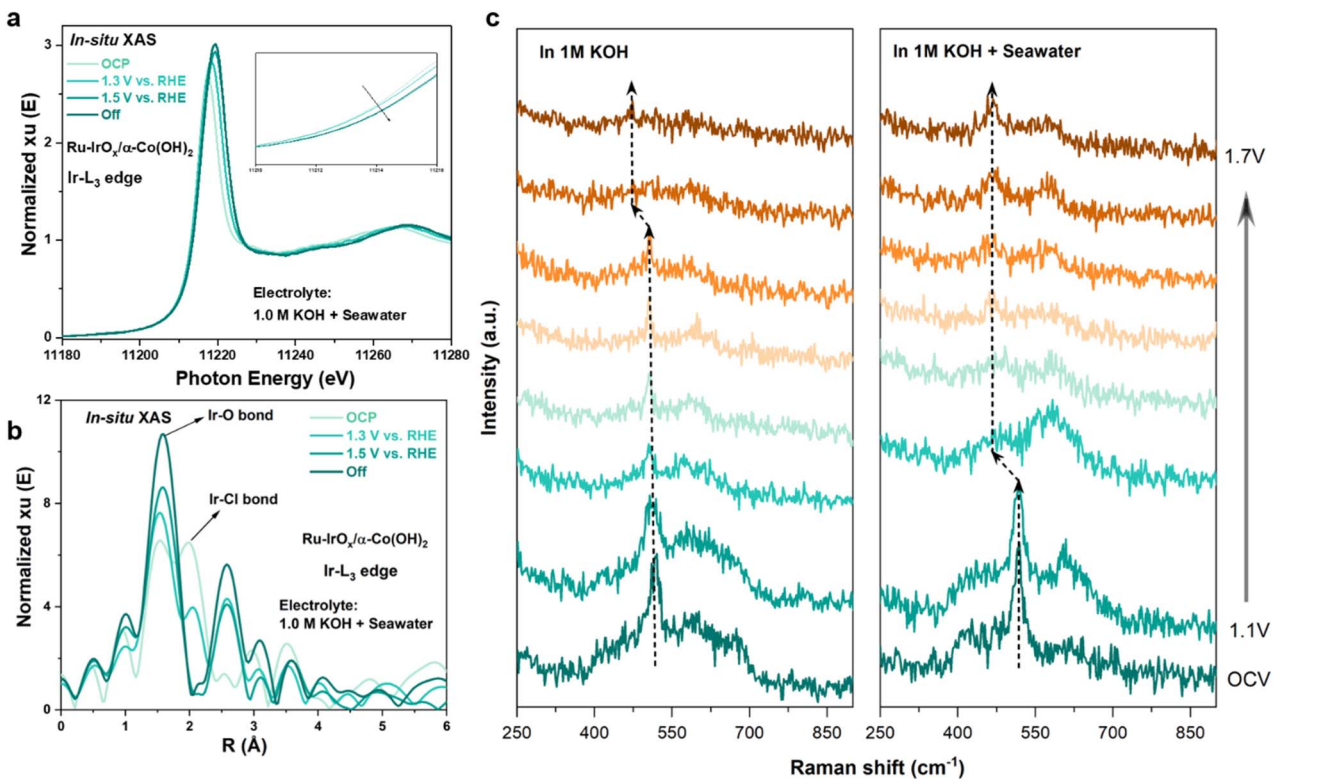

Fig. 4 *In situ* XAS and Raman analysis. (a) The XANES spectra of the Ir-L_3 edge for the Ru-IrO_x/α-$Co(OH)_2$ heterostructure under the operating voltages of OCP, 1.30 V *vs.* RHE, 1.50 V *vs.* RHE and off potential. (b) EXAFS spectra of the Ir-L_3 edge for the Ru-IrO_x/α-$Co(OH)_2$ heterostructure under the operating voltages of OCP, 1.30 V *vs.* RHE, 1.50 V *vs.* RHE and off potential. (c) *In situ* Raman spectra of the Ru-IrO_x/α-$Co(OH)_2$ heterostructure in 1 M KOH and 1 M KOH + Seawater.

voltages, suggesting that the intensity of Ir–Cl bonds weakened from OCP to 1.3 V and 1.5 V until the voltage was cut off. The phenomena can be ascribed to weakened Cl^- adsorption capacity of IrO_x clusters at high operating voltage, which favors fast OER kinetics and preventing the competing CLOR. In contrast, the intensity of Ir–O bonds exhibited a strengthened trend from OCP to higher operating potentials, suggesting more oxygen species adsorbing onto Ir sites for the OER to proceed.

Moreover, *in situ* Raman spectroscopy was performed to investigate the structural change of Ru-IrO_x/α-$Co(OH)_2$ during alkaline seawater oxidation catalysis. As shown in Fig. 4c, with the operating voltage increasing from OCV to 1.5 V *vs.* RHE, the E_g vibration signal shifts from ~515 cm^{-1} to ~469 cm^{-1}, indicating $Co(OH)_2$ gradually transformed to CoOOH,[39] which is an irreversible process. This finding was further confirmed by the XRD pattern after OER stability tests (Fig. S22), where the characteristic peaks of CoOOH appeared,[40–43] while the characteristic peaks of $Co(OH)_2$ disappeared. In 1.0 M KOH, phase transformation finished at 1.5 V *vs.* RHE, while in alkaline seawater, the phase transition started at 1.2 V *vs.* RHE, suggesting seawater benefits the phase transformation of Ru-IrO_x/α-$Co(OH)_2$ to generate more active sites.

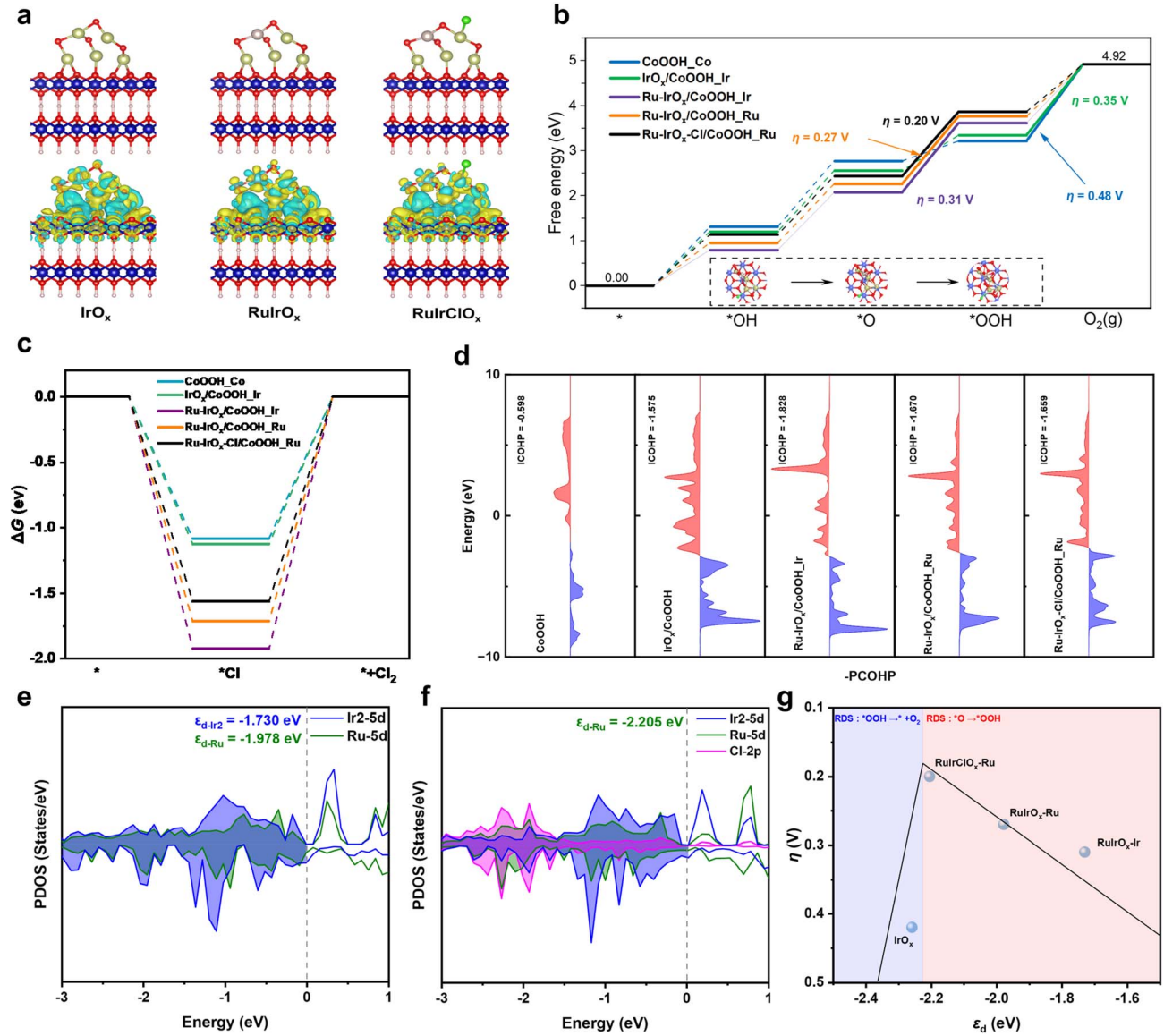

Fig. 5 Density functional theory (DFT) calculations. (a) Side view and corresponding charge density difference for IrO_x/CoOOH, Ru-IrO_x/CoOOH, and Ru-IrO_x-Cl/CoOOH. The color coding for elements is as follows: Co (blue), O (red), H (white), Ir (light green), Ru (pink), and Cl (green). Gibbs free energy diagrams for (b) the OER and (c) CLOR on CoOOH_Co, IrO_x/CoOOH_Ir, Ru-IrO_x/CoOOH_Ir, Ru-IrO_x/CoOOH_Ru, and Ru-IrOx-Cl/CoOOH_Ru. (d) Calculated COHP for *OH adsorption on CoOOH_Co, IrO_x/CoOOH_Ir, Ru-IrO_x/CoOOH_Ir, Ru-IrO_x/CoOOH_Ru, and Ru-IrO_x-Cl/CoOOH_Ru. (e) Calculated PDOS diagram for Ru-IrO_x/CoOOH. (f) Calculated PDOS diagram for Ru-IrO_x-Cl/CoOOH. (g) Calculated volcano plot illustrating the relationship between overpotential (η) and the d-band center (ε_d) for IrO_x/CoOOH_Ir, Ru-IrO_x/CoOOH_Ir, Ru-IrO_x/CoOOH_Ru, and Ru-IrO_x-Cl/CoOOH_Ru.

DFT calculations

To further elucidate the Cl^--induced phase transformation and the generation of catalytically active sites, first-principles calculations were performed. We first calculated the adsorption energies of Cl^- ions on different sites, including α-$Co(OH)_2$_Co (Co site in α-$Co(OH)_2$), IrO_x/α-$Co(OH)_2$_Ir, Ru-IrO_x/α-$Co(OH)_2$_Ru, and Ru-IrO_x/α-$Co(OH)_2$_Ir, to determine the most favorable adsorption configuration (Fig. S23). Among these, Ru-IrO_x/α-$Co(OH)_2$_Ir exhibits the lowest Cl^- adsorption energy, suggesting that Cl^- preferentially adsorbs on Ir sites, which is consistent with the XAS analysis (Fig. 4b). Experimental characterization has confirmed the transformation of the catalyst support from $Co(OH)_2$ to CoOOH, and previous reports suggest that Cl^- adsorption can promote this phase transition. To further validate this effect, we calculated the energy barriers of the phase transition from Ru-IrO_x/α-$Co(OH)_2$ to Ru-IrO_x/CoOOH under three conditions: without Cl^- adsorption, with Cl^- adsorbed on Ir, and with Cl^- adsorbed on the substrate (Fig. S24). The corresponding atomic configurations are shown in Fig. S25. The results clearly demonstrate that Cl^- adsorption significantly lowers the energy barrier of the phase transition, thereby facilitating the conversion to Ru-IrO_x/CoOOH. Charge density difference analyses were subsequently conducted for IrO_x/CoOOH, Ru-IrO_x/CoOOH, and Ru-IrO_x/CoOOH with Cl^- adsorption (denoted as Ru-IrO_x-Cl/CoOOH), as presented in Fig. 5a. Positive and negative charge redistributions are illustrated in yellow and green, respectively. Incorporation of atomically dispersed Ru into IrO_x clusters induces conformational changes and results in Ru atoms accumulating more positive charge compared with Ir. Notably, while the overall cluster structure remains stable after Cl^- adsorption on the Ir site adjacent to Ru, the electronic structure of Ru undergoes significant reconfiguration. The Bader charge calculations show that after Ru doping the positive charge of nearby Ir species decreased, while the positive charge of nearby Co species increased (Fig. S26). The DFT calculation results are consistent with the experimental observation by XPS.

The Gibbs free energy profiles for the OER process on different catalysts are shown in Fig. 5b, with the corresponding reaction intermediates illustrated in Fig. S27–S29. For Ru-IrO_x/CoOOH, the rate-determining step (RDS) is *O → *OOH, whereas for CoOOH and IrO_x/CoOOH, the RDS is *OOH → O_2. The calculated OER overpotentials are 0.48 V for CoOOH, 0.35 V for IrO_x/CoOOH, 0.31 V for Ru-IrO_x/CoOOH_Ir, and 0.27 V for Ru-IrO_x/CoOOH_Ru. Comparisons of the RDS energy barriers reveal that Ru-IrO_x/CoOOH_Ru exhibits the lowest barrier, indicating Ru as the most favorable active site. Moreover, Ru doping reduces the energy barrier at Ir sites, highlighting the synergistic effect between Ru and Ir. Due to the plausible existence of multiple species in our as-synthesized Ru-IrO_x/α-$Co(OH)_2$ catalyst, including pure IrO_x clusters (IrO_x/$Co(OH)_2$), Ru doped IrO_x (Ru-IrO_x/$Co(OH)_2$), and Co doped IrO_x (Co-IrO_x/$Co(OH)_2$), as well as atomically dispersed Ru and Ir decorating the surface of α-$Co(OH)_2$ (Ru–$Co(OH)_2$ and Ir–$Co(OH)_2$), we constructed corresponding models (Fig. S31) and calculated their Gibbs energy profiles for the OER process (Fig. S30). It is found that the RDS energy barrier was the lowest on Ru-IrO_x/$Co(OH)_2$, indicating that the Ru-IrO_x site plays a leading role during the OER and our discussions based on the Ru-IrO_x site in CoOOH are reasonable. When Cl^- is adsorbed on the Ir site adjacent to Ru (Ru-IrO_x-Cl/CoOOH_Ru), the RDS barrier is further lowered relative to Ru-IrO_x/CoOOH_Ru (Fig. 5b), suggesting that Cl^--induced electronic reconfiguration enhances OER activity. Importantly, the preferential adsorption of Cl^- on Ir prevents competition with OER active Ru sites. In contrast, Gibbs free energy profiles for the CLOR pathway (Fig. 5c) indicate that Ru-doped IrO_x clusters effectively suppress the CLOR process.

To correlate the catalyst structure with activity, crystal orbital hamilton population (COHP) analyses were conducted (Fig. S32). The electronic states of *OH intermediates on CoOOH_Co, IrO_x/CoOOH_Ir, Ru-IrO_x/CoOOH_Ir, Ru-IrO_x/CoOOH_Ru, and Ru-IrO_x-Cl/CoOOH_Ru are shown in Fig. 5d. More negative integrated (ICOHP) values indicate stronger bonding between intermediates and the catalyst. The ICOHP values of CoOOH, IrO_x/CoOOH_Ir, Ru-IrO_x/CoOOH_Ir, Ru-IrO_x/CoOOH_Ru, and Ru-IrO_x-Cl/CoOOH_Ru are −0.598, −1.575, −1.828, −1.670, and −1.659, respectively. Although stronger binding accelerates O–H bond polarization and dissociation, excessively strong adsorption hinders O–O coupling and product desorption, thereby reducing reaction kinetics. Projected density of states (PDOS) analyses (Fig. 5e, f and S33) reveal that both Ru and Ir retain abundant electronic states near the Fermi level (−1.0 to 0.0 eV), implying high reactivity. In particular, Ru-IrO_x-Cl/CoOOH shows significant overlap between Ir 5d and Cl 2p orbitals in the range of −3.0 to −2.0 eV (Fig. 5f), confirming that Cl^- adsorption modifies the Ir electronic structure. The d-band center analysis further supports these findings. The calculated values for IrO_x/CoOOH_Ir, Ru-IrO_x/CoOOH_Ir, and Ru-IrO_x/CoOOH_Ru are −2.259, −1.730, and −1.978 eV, respectively. Ru doping shifts the d-band center of adjacent Ir to less negative values, strengthening its adsorption capability. Consequently, Cl^- preferentially adsorbs on Ir. Moreover, Cl^- adsorption on Ir tunes the d-band center of neighboring Ru to −2.205 eV, optimizing its adsorption of intermediates. The correlation between d-band centers and overpotentials shown in Fig. 5g demonstrates that stronger adsorption shifts the RDS to *O → *OOH, while weaker adsorption favors *OOH → O_2. Overall, the combined effects of Ru doping and Cl^- adsorption on Ir sites adjacent to Ru significantly enhance OER activity, positioning Ru-IrO_x-Cl/CoOOH closer to the apex of the OER activity volcano plot.

Electrolyzer performance

An anion exchange membrane (AEM) electrolyzer was assembled using our as-synthesized Ru-IrO_x/α-$Co(OH)_2$ catalyst serving as the anode and a commercial Pt/C catalyst serving as the cathode. This system required a working voltage of 2.30 V to deliver 1 A cm^{-2} in the electrolyte of 1.0 M KOH + seawater, while the benchmark commercial Pt/C ‖ commercial IrO_2 coupled system required a voltage higher than 3.05 V to drive

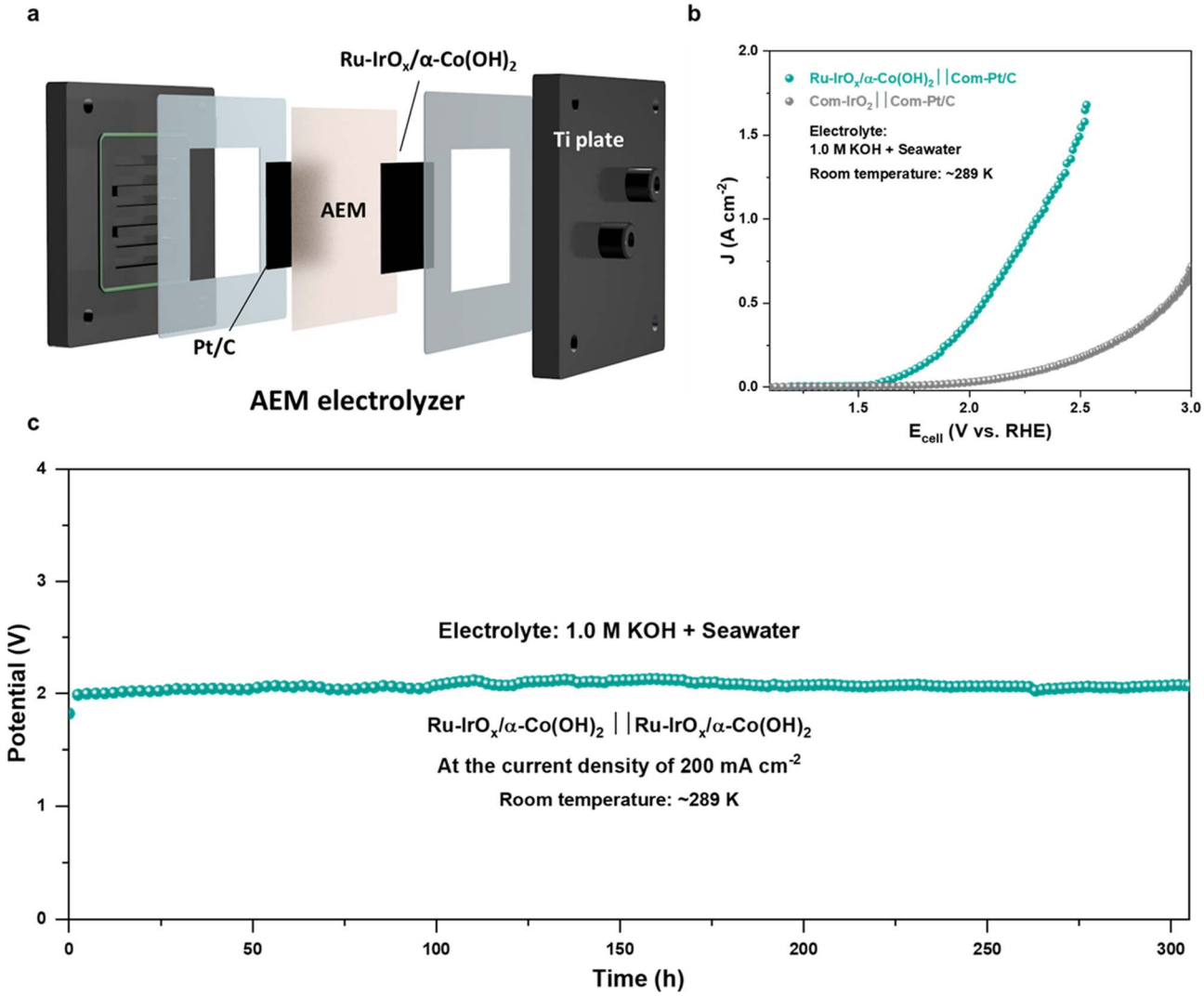

Fig. 6 AEM electrolyzer performance evaluation. (a) Schematic illustration of the anion exchange membrane electrolyzer. (b) OER activity comparison of the Ru-IrO_x/α-$Co(OH)_2$ || commercial Pt/C electrolyzer system and commercial Pt/C || commercial IrO_2 coupled electrolyzer system in the electrolyte of 1.0 M KOH + seawater. (c) The durability measurement of the Ru-IrO_x/α-$Co(OH)_2$ || commercial Pt/C system in 1.0 M KOH + seawater at the constant current density of 200 mA cm^{-2}. The AEM electrocatalysis was carried out at room temperature (~289 K).

the same current density (Fig. 6b). And the Ru-IrO_x/α-$Co(OH)_2$ || commercial Pt/C AEM system can sustain more than 300 h of electrolysis at 200 mA cm^{-2} (Fig. 6c) in 1.0 M KOH + seawater, indicating the promising potential of our as-synthesized Ru-IrO_x/α-$Co(OH)_2$ catalyst toward large-scale green hydrogen production from electrochemical seawater splitting coupled with renewable energy generation systems.

Conclusion

In conclusion, we have shown that chloride ion adsorption can significantly enhance the OER in seawater splitting by promoting phase transformation in the catalyst. The Ru-IrO_x/α-$Co(OH)_2$ heterostructure catalyst, consisting of atomically dispersed Ru-doped IrO_x nanoclusters on α-$Co(OH)_2$ nanosheets, achieved a low overpotential of only 200 mV to drive a current density of 100 mA cm^{-2}, and it remained stable for 310 hours at 500 mA cm^{-2}. *In situ* spectroscopy and theoretical calculations revealed that at low overpotentials, Cl^- ion adsorption on IrO_x clusters induces the phase transformation of α-$Co(OH)_2$ to CoOOH, lowering the OER barrier at the Ru site. This phase transition, facilitated by Cl^- ions, resulted in a significantly reduced theoretical overpotential of 200 mV for the Ru-IrO_x-Cl/CoOOH catalyst. Our findings demonstrate a novel approach to seawater splitting, where chloride ion adsorption promotes catalytic activity, contrasting with traditional chloride-repelling catalyst strategies.

Author contributions

H. Ma, Y. Jin and X. Zhou contributed equally to this work. H. Ma, H. Cheng, J. Ma, E. Song and W. Huang conceived the research project. H. Cheng, J. Ma, E. Song and W. Huang supervised the project. H. Ma designed and fabricated the

catalysts, performed most of the experiments and conducted detailed analysis of experimental data. W. Huang conducted both *in situ* and *ex situ* XAS measurements, and contributed a lot to all the XAS data analysis. Y. Jin performed the density functional theory simulations and provided solid evidence to explain the experimental findings under the supervisor of E. Song. X. Zhou and Y. Cui conducted some part of the experiments and provided solid assistance in completing this project. Y. Zhao conducted the spherical aberration corrected transmission electron microscopy test and carefully analyzed the relevant characterization results. C. Chang and M. Yeh assisted in both the *in situ* and *ex situ* XAS measurements, and contributed to some XAS data analysis.

Conflicts of interest

There are no conflicts to declare.

Data availability

The data that support the findings of this study are available from the corresponding authors upon reasonable request. All supporting data including experiment and calculation methods, materials characterization details, XAS analyais details, electrochemical test data and calculation results details are available in the supplementary information (SI). Supplementary information: additional data. See DOI: https://doi.org/10.1039/d5sc09403h.

Acknowledgements

This work was funded by the National Natural Science Foundation of China (22405191), Natural Science Foundation of Shanghai Municipality (24ZR1468100) and the Fundamental Research Funds for the Central Universities to H. Cheng. The authors acknowledge the XAS resource provided by the National Synchrotron Radiation Research Center (NSRRC) in Taiwan and the Spherical Aberration Corrected Transmission Electron Microscope (AC-TEM) provided by Dalian Institute of Chemical Physics, Chinese Academy of Sciences, China. The authors also acknowledge the computational resources provided by Shanghai Institute of Ceramics, Chinese Academy of Sciences, China. We acknowledge funding from the Scientific Research Innovation Capability Support Project for Young Faculty (ZYGXQNJSKYCXNLZCXM-E10) and support from the Xiaomi Young Talents Program. We thank the Taiwan Light Source (TLS) (beamline 17A1) for the allocation of synchrotron beam time under Proposal No. 2024-2-027-1.

Notes and references

1 D. Li, E. J. Park, W. Zhu, Q. Shi, Y. Zhou, H. Tian, Y. Lin, A. Serov, B. Zulevi, E. D. Baca, C. Fujimoto, H. T. Chung and Y. S. Kim, *Nat. Energy*, 2020, **5**, 378–385.
2 H. Xie, Z. Zhao, T. Liu, Y. Wu, C. Lan, W. Jiang, L. Zhu, Y. Wang, D. Yang and Z. Shao, *Nature*, 2022, **612**, 673–678.
3 J. Guo, Y. Zheng, Z. Hu, C. Zheng, J. Mao, K. Du, M. Jaroniec and S.-Z. Qiao, *Nat. Energy*, 2023, **8**, 264–272.
4 H. Jin, J. Xu, H. Liu, H. Shen, H. Yu, M. Jaroniec, Y. Zheng and S.-Z. Qiao, *Sci. Adv.*, 2023, **9**, eadi7755.
5 X. Kang, F. Yang, Z. Zhang, H. Liu, S. Ge, S. Hu, S. Li, Y. Luo, Q. Yu, Z. Liu, Q. Wang, W. Ren, C. Sun, H.-M. Cheng and B. Liu, *Nat. Commun.*, 2023, **14**, 3607.
6 X. Wang, X. Zhou, C. Li, H. Yao, C. Zhang, J. Zhou, R. Xu, L. Chu, H. Wang, M. Gu, H. Jiang and M. Huang, *Adv. Mater.*, 2022, **34**, 2204021.
7 F. Sun, J. Qin, Z. Wang, M. Yu, X. Wu, X. Sun and J. Qiu, *Nat. Commun.*, 2021, **12**, 4182.
8 R. Fan, C. Liu, Z. Li, H. Huang, J. Feng, Z. Li and Z. Zou, *Nat. Sustain.*, 2024, **7**, 158–167.
9 S. Zhang, X. Wei, S. Dai, H. Wang and M. Huang, *Adv. Funct. Mater.*, 2024, **34**, 2311370.
10 F. Dong, H. Duan, Z. Lin, H. Yuan, M. Ju, X. Du, J. Gao, J. Yu and S. Yang, *Appl. Catal. B: Environ.*, 2024, **340**, 123242.
11 X. Wei, S. Zhang, X. Lv, S. Dai, H. Wang and M. Huang, *Appl. Catal. B: Environ.*, 2024, **345**, 123661.
12 L. Chong, G. Gao, J. Wen, H. Li, H. Xu, Z. Green, J. D. Sugar, A. Jeremy Kropf, W. Xu, X.-M. Lin, H. Xu, L.-W. Wang and D.-J. Liu, *Science*, 2023, **380**, 609–616.
13 Y. Zhao, D. P. Adiyeri Saseendran, C. Huang, A. C. Triana, W. A. Marks, H. Chen, H. Zhao and G. R. Patzk, *Chem. Rev.*, 2023, **123**, 6257–6358.
14 B. Zhang, X. Zheng, O. Voznyy, R. Comin, M. Bajdich, M. García-Melchor, L. Han, J. Xu, M. Liu, L. Zheng, F. P. García de Arquer, C. T. Dinh, F. Fan, M. Yuan, E. Yassitepe, N. Chen, T. Regier, P. Liu, Y. Li, P. D. Luna, A. Janmohamed, H. L. Xin, H. Yang, A. Vojvodic and E. H. Sargent, *Science*, 2016, **352**, 333–337.
15 Y. Zhou, J. Hu, L. Yang and Q. Gao, *Chin. Chem. Lett.*, 2022, **33**, 2845–2855.
16 B. He, F. Bai, P. Jain and T. Li, *Small*, 2025, **21**, 2411479.
17 Z. Li, X. Zhang, Z. Zhang, P. Chen, Y. Zhang and X. Dong, *Appl. Catal. B: Environ.*, 2023, **325**, 122311.
18 Y. Zhai, X. Ren, Y. Sun, D. Li, B. Wang and S. Liu, *Appl. Catal. B: Environ.*, 2023, **323**, 122091.
19 X. Duan, Q. Sha, P. Li, T. Li, G. Yang, W. Liu, E. Yu, D. Zhou, J. Fang, W. Chen, Y. Chen, L. Zheng, J. Liao, Z. Wang, Y. Li, H. Yang, G. Zhang, Z. Zhuang, S.-F. Hung, C. Jing, J. Luo, L. Bai, J. Dong, H. Xiao, W. Liu, Y. Kuang, B. Liu and X. Sun, *Nat. Commun.*, 2024, **15**, 1973.
20 H. Yu, J. Wan, M. Goodsite and H. Jin, *One Earth*, 2023, **6**, 267–277.
21 Y. Yu, W. Zhou, X. Zhou, J. Yuan, X. Zhang, L. Wang, J. Li, X. Meng, F. Sun, J. Gao and G. Zhao, *ACS Catal.*, 2024, **14**, 18322–18332.
22 J. G. Vos, T. A. Wezendonk, A. W. Jeremiasse and M. T. M. Koper, *J. Am. Chem. Soc.*, 2018, **140**, 10270–10281.
23 D. H. Kweon, M. S. Okyay, S.-J. Kim, J.-P. Jeon, H.-J. Noh, N. Park, J. Mahmood and J.-B. Baek, *Nat. Commun.*, 2020, **11**, 1278.
24 J. Mahmood, F. Li, S.-M. Jung, M. S. Okyay, I. Ahmad, S.-J. Kim, N. Park, H. Y. Jeong and J.-B. Baek, *Nat. Nano.*, 2017, **12**, 441–446.

25 Z.-L. Wang, K. Sun, J. Henzie, X. Hao, C. Li, T. Takei, Y.-M. Kang and Y. Yamauchi, *Angew. Chem., Int. Ed.*, 2018, **57**, 5848–5852.
26 X. Zheng, J. Yang, Z. Xu, Q. Wang, J. Wu, E. Zhang, S. Dou, W. Sun, D. Wang and Y. Li, *Angew. Chem., Int. Ed.*, 2022, **61**, e202205946.
27 D. Liu, Q. Lv, S. Lu, J. Fang, Y. Zhang, X. Wang, Y. Xue, W. Zhu and Z. Zhuang, *Nano Lett.*, 2021, **21**, 2809–2816.
28 R. Jin, M. Peng, A. Li, Y. Deng, Z. Jia, F. Huang, Y. Ling, F. Yang, H. Fu, J. Xie, X. Han, D. Xiao, Z. Jiang, H. Liu and D. Ma, *J. Am. Chem. Soc.*, 2019, **141**, 18921–18925.
29 Z. Lei, W. Cai, Y. Rao, K. Wang, Y. Jiang, Y. Liu, X. Jin, J. Li, Z. Lv, S. Jiao, W. Zhang, P. Yan, S. Zhang and R. Cao, *Nat. Commun.*, 2022, **13**, 24.
30 R.-Q. Yao, H. Shi, W.-B. Wan, Z. Wen, X.-Y. Lang and Q. Jiang, *Adv. Mater.*, 2020, **32**, 1907214.
31 Y. Dou, C.-T. He, L. Zhang, H. Yin, M. Al-Mamun, J. Ma and H. Zhao, *Nat. Commun.*, 2020, **11**, 1664.
32 Z.-Y. Wu, F.-Y. Chen, B. Li, S.-W. Yu, Y. Z. Finfrock, D. M. Meira, Q.-Q. Yan, P. Zhu, M.-X. Chen, T.-W. Song, Z. Yin, H.-W. Liang, S. Zhang, G. Wang and H. Wang, *Nat. Mater.*, 2023, **22**, 100–108.
33 W. Wei, Z. Wei, R. Li, Z. Li, R. Shi, S. Ouyang, Y. Qi, D. L. Philips and H. Yuan, *Nat. Commun.*, 2022, **13**, 3199.
34 Y. Zhu, L. Zhang, B. Zhao, H. Chen, X. Liu, R. Zhao, X. Wang, J. Liu, Y. Chen and M. Liu, *Adv. Funct. Mater.*, 2019, **29**, 1901783.
35 Y. Xue, B. Huang, Y. Yi, Y. Guo, Z. Zuo, Y. Li, Z. Jia, H. Liu and Y. Li, *Nat. Commun.*, 2018, **9**, 1460.
36 H. Su, W. Zhou, W. Zhou, Y. Li, L. Zheng, H. Zhang, M. Liu, X. Zhang, X. Sun, Y. Xu, F. Hu, J. Zhang, T. Hu, Q. Liu and S. Wei, *Nat. Commun.*, 2021, **12**, 6118.
37 W. H. Lee, M. H. Han, Y.-J. Ko, B. K. Min, K. H. Chae and H.-S. Oh, *Nat. Commun.*, 2022, **13**, 605.
38 X. Xie, L. Du, L. Yan, S. Park, Y. Qiu, J. Sokolowski, W. Wang and Y. Shao, *Adv. Funct. Mater.*, 2022, **32**, 2110036.
39 P. Gao, Y. Zeng, P. Tang, Z. Wang, J. Yang, A. Hu and J. Liu, *Adv. Funct. Mater.*, 2022, **32**, 2108644.
40 J. Huang, J. Chen, T. Yao, J. He, S. Jiang, Z. Sun, Q. Liu, W. Cheng, F. Hu, Y. Jiang, Z. Pan and S. Wei, *Angew. Chem., Int. Ed.*, 2015, **54**, 8722–8727.
41 J. Y. Park, H. Y. Kim, Y.-I. Kim, S. Y. Jo, S. A. Abbas, D. Seo, A. Ma and K. M. Nam, *J. Mater. Chem. A*, 2022, **10**, 12047–12054.
42 T. Zhang, J. Jiang, W. Sun and D. Wang, *Proc. Natl. Acad. Sci. U. S. A.*, 2024, **121**, e2317247121.
43 L. Tang, M. Xia, S. Cao, X. Bo, S. Zhang, Y. Zhang, X. Liu, L. Zhang, L. Yu and D. Deng, *Nano Energy*, 2022, **101**, 107562.